An ATP-dependent partner switch links flagellar C-ring assembly with gene expression

Vitan Blagotinsek[a,b,1], Meike Schwan[c,1], Wieland Steinchen[a,b], Devid Mrusek[a,b], John C. Hook[c], Florian Rossmann[c,d], Sven A. Freibert[e], Hanna Kratzat[f,g], Guillaume Murat[h], Dieter Kressler[h], Roland Beckmann[f,g], Morgan Beeby[d], Kai M. Thormann[c,2], and Gert Bange[a,b,2]

[a]Center for Synthetic Microbiology (SYNMIKRO), Philipps-University Marburg, 35043 Marburg, Germany; [b]Department of Chemistry, Philipps-University Marburg, 35043 Marburg, Germany; [c]Department of Microbiology and Molecular Biology, Justus-Liebig-Universität, 35392 Giessen, Germany; [d]Department of Life Sciences, Imperial College London, London SW7 2AZ, United Kingdom; [e]Institut für Zytobiologie und Zytopathologie, Philipps-Universität Marburg, 35032 Marburg, Germany; [f]Genzentrum, Ludwig-Maximilians-Universität, 81377 Munich, Germany; [g]Department of Biochemistry, Ludwig-Maximilians-Universität, 81377 Munich, Germany; and [h]Department of Biology, University of Fribourg, 1700 Fribourg, Switzerland

Bacterial flagella differ in their number and spatial arrangement. In many species, the MinD-type ATPase FlhG (also YlxH/FleN) is central to the numerical control of bacterial flagella, and its deletion in polarly flagellated bacteria typically leads to hyperflagellation. The molecular mechanism underlying this numerical control, however, remains enigmatic. Using the model species *Shewanella putrefaciens*, we show that FlhG links assembly of the flagellar C ring with the action of the master transcriptional regulator FlrA (named FleQ in other species). While FlrA and the flagellar C-ring protein FliM have an overlapping binding site on FlhG, their binding depends on the ATP-dependent dimerization state of FlhG. FliM interacts with FlhG independent of nucleotide binding, while FlrA exclusively interacts with the ATP-dependent FlhG dimer and stimulates FlhG ATPase activity. Our in vivo analysis of FlhG partner switching between FliM and FlrA reveals its mechanism in the numerical restriction of flagella, in which the transcriptional activity of FlrA is down-regulated through a negative feedback loop. Our study demonstrates another level of regulatory complexity underlying the spationumerical regulation of flagellar biogenesis and implies that flagellar assembly transcriptionally regulates the production of more initial building blocks.

flagellum | ATPase | regulation | nanomachine | spatiotemporal

Many bacteria use flagella for motility. The core flagellar architecture is conserved and is composed of a cytoplasmic C ring, basal body, rod, and extracellular hook and filament (1, 2). Nevertheless, the number and arrangement of flagella differ between species (3, 4) through molecular mechanisms that are only poorly understood.

In polar flagellates, the MinD-type ATPase FlhG (synonyms: FleN, YlxH, and MinD2) restricts the number of polar flagella. Deletion of *flhG* leads to hyperflagellated cells with decreased motility in *Pseudomonas aeruginosa* (FleN is the name of the *P. aeruginosa* FlhG homolog) (5), *Vibrio cholerae* and *Vibrio alginolyticus* (6, 7), and *Shewanella putrefaciens* (8). In the distantly related amphitrichous flagellate food pathogen *Campylobacter jejuni*, deletion of *flhG* similarly increases the number of flagella and reduces motility (9). How FlhG moderates the number of flagella, however, remains unclear.

FlhG is homologous to the MinD/ParA-type ATPases and shares significant structural and functional similarity (8, 10); indeed, in *C. jejuni* FlhG plays the role of MinD in determining the site of cell division (11). Like MinD (12, 13), FlhG forms ATP-dependent homodimers that interact with the inner membrane through a C-terminal amphipathic helix or a membrane-targeting sequence (MTS) (8, 10). FlhG acts in concert with the signal recognition particle–GTPase FlhF and stimulates the GTPase activity of FlhF (14–16). FlhG also interacts with the N terminus of the flagellar C-ring protein FliM in polarly flagellated bacteria (8). In *S. putrefaciens*, the N terminus of FliM contains a highly conserved motif (amino acid EIDAL), which is necessary and sufficient to interact with FlhG. The *P. aeruginosa* FlhG homolog FleN binds to the flagellar transcriptional master regulator FleQ (17) and is required for FleQ inhibition by the second messenger c-di-GMP (18). Taken together, studies show that FlhG switches between a monomeric and homodimeric state in an ATP-dependent manner and interacts with phospholipids in its ATP-bound homodimeric state as well as with FlhF, FliM, or FleQ. The interplay and functional consequences of those features, however, are far from being understood. Here we sought to explore the molecular mechanism underlying the numerical regulation of flagella by FlhG in monopolarly flagellated bacteria, using *S. putrefaciens* as a model system.

Results

FlhG Is Passively Transported by FliM/FliN to the Assembling Flagellar C Ring. We first developed a suitable strain to study the mechanism of FlhG. To focus exclusively on the polar flagellum of *S. putrefaciens,* we disabled its lateral flagellar system, used for movement through structured environments and with auxiliary roles in free swimming (19, 20), by deleting its lateral flagellins ($\Delta flaAB_2$). Because FlhG has been implicated to interact with the C ring (8), we also sought to determine whether polar flagella in our hyperflagellated Δ*flhG* strain assemble correctly. We compared

Significance

Flagella, bacterial organelles of locomotion, appear in a defined number and localization at the bacterial cell surface. The MinD-type ATPase FlhG numerically regulates flagellation patterns through a molecular mechanism only poorly understood. Depending on its ATP-dependent oligomerization state, FlhG interacts either with the C-ring protein FliM during flagellar assembly or with flagellar master regulator FlrA. This partner switch between FliM and FlrA establishes a regulatory network critical for the numerical regulation of flagella, in which the physical assembly of the flagellum transcriptionally feeds back to prevent the production of more building blocks.

Author contributions: D.K., K.M.T., and G.B. designed research; V.B., M.S., W.S., D.M., J.C.H., F.R., S.A.F., H.K., and G.M. performed research; R.B. contributed new reagents/analytic tools; V.B., M.S., W.S., D.M., F.R., S.A.F., M.B., K.M.T., and G.B. analyzed data; and M.B., K.M.T., and G.B. wrote the paper.

The authors declare no competing interest.

[1]V.B. and M.S. contributed equally to this work.

[2]To whom correspondence may be addressed. Email: Kai.Thormann@mikro.bio.uni-giessen.de or gert.bange@synmikro.uni-marburg.de.

flagellar basal bodies in wild-type (wt) and Δ*flhG* mutant strains of *S. putrefaciens* in situ by electron cryotomography (cryo-ET). The wt *S. putrefaciens* motor resembled other flagellar motors from unsheathed, polar flagellated γ-proteobacteria such as *S. oneidensis* (21) and *Plesiomonas shigelloides* (22). The structure of hyperflagellated Δ*flhG S. putrefaciens* C rings was indistinguishable from those of the wt, confirming that flagellar C-ring assembly is unaffected by deletion of FlhG and demonstrating that FlhG is neither crucial for proper C-ring assembly nor an integral part of it (Fig. 1*A* and *SI Appendix*, Fig. S1).

FlhG interacts with the conserved N-terminal EIDAL motif of the C-ring protein FliM (8). We used fluorescence microscopy on a Δ*flhG* strain that encodes fluorescently labeled FliM and FlhG (FliM-mCherry and FlhG-GFP). Both proteins colocalized to the flagellated cell pole (Fig. 1 *B*, *Upper*). Upon deletion of the FlhG-binding site on FliM ($FliM_{\Delta N}$-mCherry), $FliM_{\Delta N}$-mCherry still localized to the flagellated cell pole, but FlhG-GFP was evenly distributed throughout the cytoplasm, no longer colocalizing to the flagellar pole (Fig. 1 *B*, *Lower*). We conclude that FlhG does not determine the polar localization of the flagellar C ring and is apparently not required for the assembly of flagella (Fig. 1*A*). On the contrary, that FliM is required for polar localization of FlhG indicates that FlhG is transported with FliM to the assembling C ring at the base of the nascent flagellum.

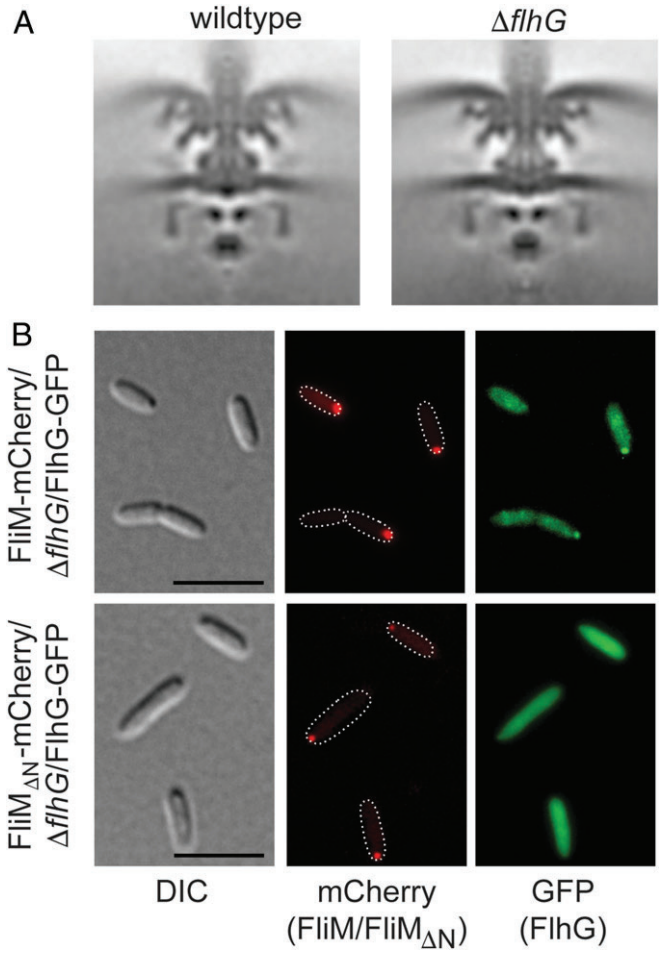

Fig. 1. FliM and FlhG in the context of the C-ring assembly. (*A*) Cryo-ET images showing 100 × 100 nm slices through symmetrized subtomogram averages of the *S. putrefaciens* wt (*Left*) and Δ*flhG* motor (*Right*). (*B*) Fluorescence and DIC microscopy images depicting FliM-mCherry/Δ*flhG*/FlhG-GFP localization (*Upper*) and FliM-Δ*N*-mCherry/Δ*flhG*/FlhG-GFP (*Lower*). (Scale bar, 5 μm.)

The ATP-Dependent FlhG Homodimer Interacts with FlrA. If FlhG is only passively transported by FliM to the flagellar cell pole and is not fundamental for C-ring assembly, what is its role at the flagellar assembly site? In *P. aeruginosa*, the FlhG homolog FleN interacts with FleQ (17), which inversely regulates flagella assembly and exopolysaccharide production (23–25). We speculated that a similar interaction also occurs between FlhG and the FleQ homolog FlrA in *S. putrefaciens*. We performed yeast two-hybrid (Y2H) assays in order to assess the interaction of FlhG with FlrA and other predicted binding partners in *S. putrefaciens*. Indeed, FlhG interacted with FlrA, as well as FliM and FlhF, but not with the negative controls FliG and FliN (Fig. 2*A*) (8, 14).

FlrA is a three-domain protein consisting of a receiver (Rec) followed by an AAA+-type ATPase and an HTH domain that typically binds DNA (Fig. 2*B*). To determine which of the FlrA domains would bind to FlhG, we performed in vitro glutathione-S-transferase (GST) pulldown assays with GST-fusion proteins of the FlrA Rec, AAA-HTH, or HTH domains. In the presence of ATP we detected an interaction of FlhG with the AAA-HTH and HTH domains of FlrA (Fig. 2*C*), suggesting that FlrA's HTH domain primarily mediates interaction with the ATP-dependent FlhG homodimer. We performed further pulldown assays employing a strictly homodimeric variant of FlhG ($FlhG_{D58A}$), which interacts with the AAA-HTH and HTH domains of FlrA even without ATP (*SI Appendix*, Fig. S2*A*), in contrast to the native FlhG requiring ATP (*SI Appendix*, Fig. S2*B*). We conclude that the ATP-dependent homodimeric state of FlhG is a prerequisite for its interaction with the HTH domain of FlrA.

FlhG Binds a Disordered N-Terminal Region of the FlrA HTH Domain. We aimed to define the region of the FlrA HTH domain bound by FlhG. In silico analysis of our FlrA-HTH construct revealed a putative N-terminal short α-helix and a disordered loop (together named "linker") included in our HTH domain construct and not part of the AAA+ domain (Fig. 2*B*). In vitro the GST-tagged FlrA HTH domain including this linker (residues: 375 to 477) pulled down FlhG in the presence of ATP (Fig. 2*D*). To probe the role of the linker, we then truncated its N terminus by 16 or 36 amino acids ($HTH_{\Delta N16}$ and $HTH_{\Delta N36}$, respectively). GST-$HTH_{\Delta N16}$, but not GST-$HTH_{\Delta N36}$, still interacted with FlhG (Fig. 2*D*), indicating that FlhG interacts with the disordered part of the linker region between the AAA+ and HTH domains of FlrA.

FlrA-HTH Stimulates FlhG ATPase Activity. We next wanted to determine the interaction strength between FlhG and FlrA-HTH. Using microscale thermophoresis (MST), we found that the dissociation constant (K_d) of FlrA-HTH and FlhG in the presence of 0.25 mM ATP was 1.6 ± 0.1 μM (Fig. 2*E*). Consistent with our pulldown results, we did not detect any interaction of FlrA-HTH with FlhG in the absence of ATP using MST (Fig. 2*E*). As FlrA-HTH only interacts with the ATP-dependent FlhG homodimer, we speculated whether FlrA-HTH might affect FlhG's ATPase activity. We assayed the ATPase activity of FlhG alone and in the presence of FlrA-HTH at different ATP concentrations (Fig. 2*F*). The ATPase activity of FlhG alone was low, with Michaelis–Menten constant (K_m) and maximum velocity (V_{max}) values of 0.45 ± 0.34 mM ATP and 0.08 ± 0.02 μM ATP hydrolyzed per minute per μM FlhG, respectively. This V_{max} agrees well with end point measurements by Schuhmacher et al. for *B. subtilis* FlhG homolog YlxH (8). Upon adding FlrA-HTH, however, V_{max} increased by about fivefold (0.48 ± 0.04 μM ATP hydrolyzed per minute per μM FlhG) with unaltered K_m (0.36 ± 0.12 mM ATP). Taken together, these results support that FlrA-HTH stimulates the ATPase activity of FlhG, suggesting that FlrA promotes a shift from the dimeric to the monomeric form of FlhG.

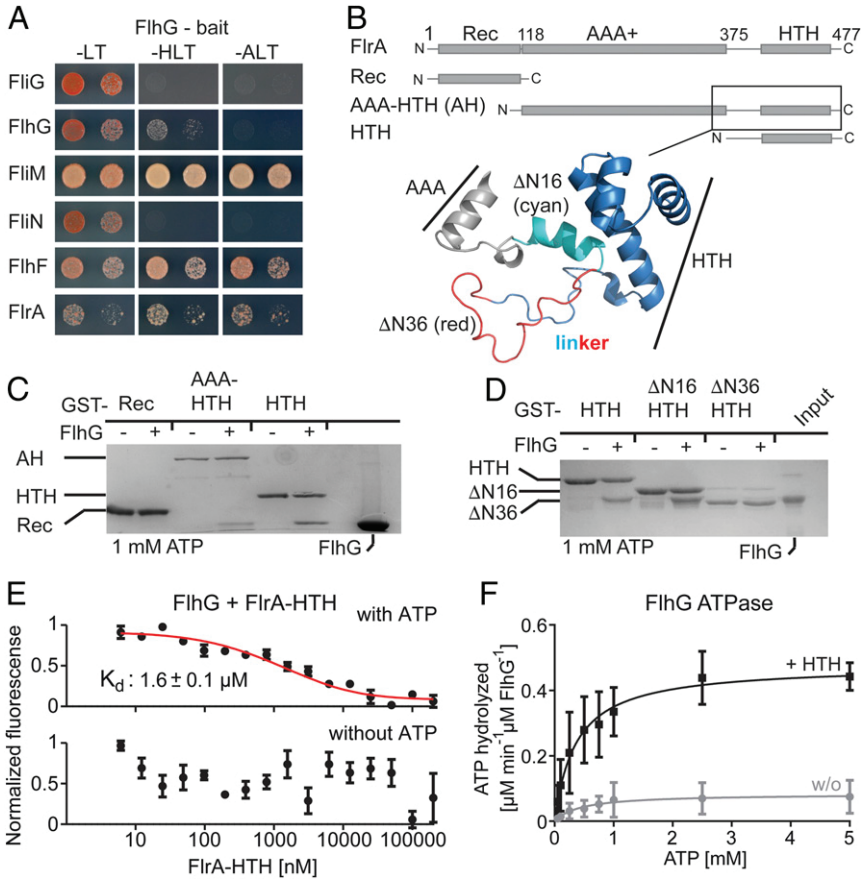

Fig. 2. Dissection of the FlhG/FlrA interaction. (*A*) Y2H experiments show that FlhG interacts with FliM, FlhF, and FlrA, but not with FliG and FliN. The growth of cells, coexpressing the FlhG bait protein and the indicated prey proteins, was assessed on -LT, -HLT (HIS3 reporter), and -ALT (ADE2 reporter) plates. (*B*) Domain architecture of FlrA (*Upper*) and structural details of the FlrA linker region and HTH domain (*Lower*); SpFlrA model based on 5m7n (NtrX from *Brucella abortus*), created with SWISS-MODEL. (*C*) Pulldown assay probing the interaction of FlrA truncations with FlhG in the presence of 1 mM ATP. (*D*) Pulldown assay probing the interaction of the FlrA-HTH domain and its preceding linker region with FlhG in the presence of 1 mM ATP. (*E*) Interaction of FlhG with the FlrA-HTH domain probed by MST in the presence of 0.25 mM ATP (*Upper*) and in its absence (*Lower*). Data represent mean ± SD of $n = 3$ technical replicates. (*F*) Velocity/substrate characteristic of FlhG ATPase activity in the absence (gray curve) or presence (black curve) of equimolar FlrA-HTH. Data represent mean ± SD of $n = 3$ technical replicates.

FliM and FlrA Share Overlapping Binding Sites at FlhG. Our finding that the FlhG interaction with FlrA depends on ATP contrasts with the ATP-independent interaction of FlhG with FliM. The K_d of FlhG for the FliM/FliN complex was 3.1 ± 0.3 μM in the absence of ATP and 6.8 ± 0.6 μM in the presence of 0.25 mM ATP (*SI Appendix*, Fig. S2*C*). Thus, the affinities for the interaction of FlhG with either FlrA or FliM are very similar.

We used hydrogen–deuterium exchange (HDX) mass spectrometry (MS) to determine where FlrA and FliM bind FlhG. In HDX, the protein under investigation is incubated in deuterated buffer either with or without a binding partner, allowing the amide hydrogens to exchange for deuterium. After digesting the proteins with pepsin the deuterium incorporation of those peptide fragments is analyzed by mass spectrometry. Differences in deuteration indicate binding surfaces or conformational changes of the protein. To determine where FlrA-HTH binds FlhG, we used the homodimeric $FlhG_{D58A}$ variant and compared its HDX profile with and without FlrA-HTH. We identified 128 peptides of $FlhG_{D58A}$, covering 92% of the protein sequence with a 4.5-fold redundancy per amino acid (Datasets S1 and S2). Multiple peptides of $FlhG_{D58A}$ incorporated less deuterium (>0.5 Da difference; ref. 26) in the presence of FlrA-HTH (Fig. 3*A* and *SI Appendix*, Fig. S3). Some of those peptides, including the loops connecting β1 and α2 and β5 and α5, are located at the intersubunit interface of the FlhG dimer, indicating a conformational change of the FlhG homodimer (Fig. 3 *A*, *Left*). This may also explain the reduced HDX of helix α6 and the β2-α4 region as they contribute to the intersubunit interface. For helix α7, however, an altered topology would not sufficiently explain its reduced HDX. Furthermore, in the context of the FlhG homodimer, α6 together with α5 and the β2-α4 region of the opposing monomer provides a groove, which may represent the binding site for FlrA-HTH on dimeric FlhG (Fig. 3 *A*, *Right*).

To determine the binding site of FliM on FlhG, we again performed HDX-MS, yielding 77 FlhG peptides covering 91.8% of the protein sequence with a 3.71-fold redundancy per amino acid (Datasets S1 and S2). Regions of FlhG with reduced HDX in the presence of the FliM/FliN complex locate to helices α6 and α7, overlapping with the binding site of FlrA-HTH (Fig. 3*B* and *SI Appendix*, Fig. S4). The β2-α4 region of FlhG, however, did not display reduced HDX, potentially explaining why FliM interacts with the monomeric of FlhG and FlrA-HTH interacts with the dimer. Interestingly, we observed regions on the dorsal side of FlhG with increased HDX in the presence of FliM/FliN, encompassing the C-terminal tip of α2, α9, and β-strands β2, β3, and β4 but not including the interconnecting loops as in the case of FlrA-HTH–FlhG interaction (Fig. 3*B*). Closer inspection of the mass spectra revealed a bimodal behavior of the peptides, suggesting that the increased HDX was due to partial unfolding of the secondary structure (*SI Appendix*, Fig. S5). We speculate

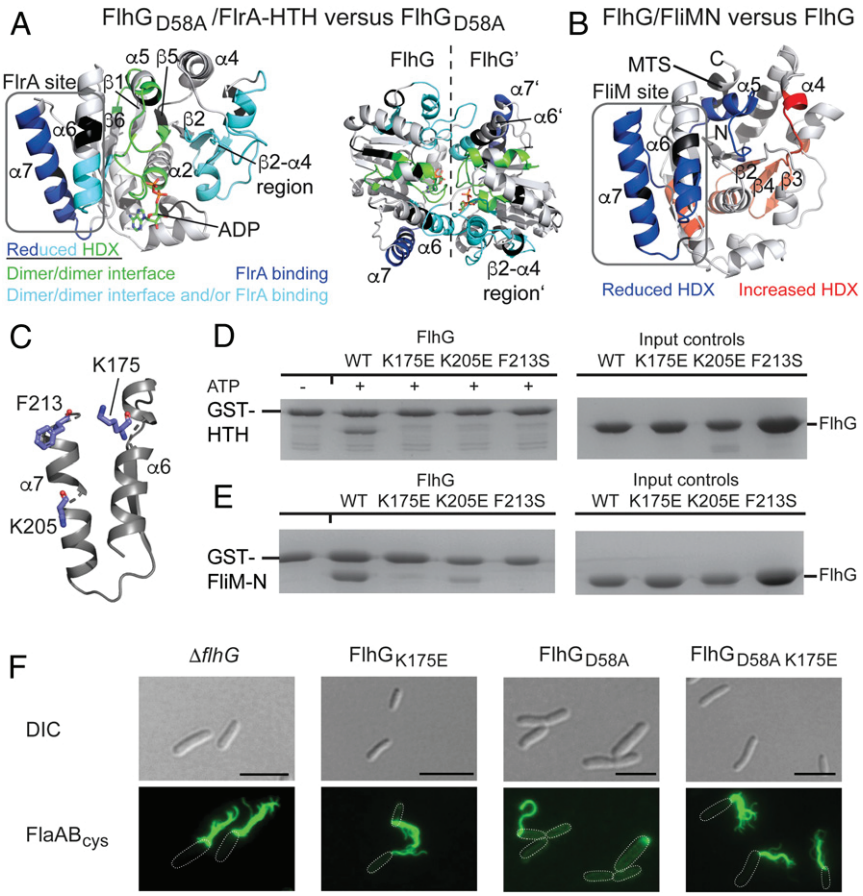

Fig. 3. FliM and FlrA share a binding site at FlhG. (*A*) Peptides exhibiting reduced HDX in the $FlhG_{D58A}$/FlrA-HTH complex are mapped onto a structural model of FlhG (generated with SWISS-MODEL based on the structure of homodimeric FlhG from *Geobacillus thermodenitrificans*; PDB ID code 4RZ3, ref. 8). The different coloring of the peptides denotes the presumed reason for the observed differences in HDX based on their implication in establishing the homodimeric interface of FlhG (green), interface establishment and/or FlrA binding (cyan), or FlrA binding (blue). (*B*) Peptides exhibiting reduced (blue) or increased (red) HDX in the FlhG/FliN complex are mapped onto a structural model of FlhG (generated with SWISS-MODEL based on the structure of monomeric FlhG from *Geobacillus thermodenitrificans*; PDB ID code 4RZ2, ref. 8). (*C*) Key residues residing in helices α6 and α7 of FlhG involved in the interaction with FliM and FlrA-HTH. (*D*) GST pulldown with an immobilized FlrA-HTH domain against FlhG single mutants (in the presence of 1 mM ATP). Mutants prevent a binding interaction. (*E*) GST pulldown with an immobilized FliM-N against FlhG single mutants (absence of ATP). Mutants prevent a binding interaction. (*F*) Fluorescence microscopy (Alexa Fluor 488 maleimide staining) and DIC microscopy images of FlhG wt and mutants, showing the change in flagellation pattern and location. $FlhG_{D58A}$ leads to loss of flagella in most cells. (Scale bar, 5 μm.)

that this observation could be explained by changes in the structurally unresolved N-terminal helix α1 or the MTS of FlhG (although we do not observe HDX differences in those) or may be a mechanism to prevent interactions between FlhG and other proteins during the colocalization with FliM to the nascent flagellar structure. Together, our HDX-MS results strongly suggest a shared binding site for FliM and FlrA-HTH on FlhG.

The Shared FliM/FlrA-Binding Site on FlhG Is Critical for Its Function. Our results showed that the FlrA- and FliM-binding sites overlap at helices α6 and α7 of FlhG (Fig. 3 *A* and *B*). Closer inspection of this region identified several residues (i.e., K175, K205, and F213) that could be involved in mediating the interaction of FlhG to either FliM or FlrA (Fig. 3*C*). We therefore generated mutants to assess the significance of these residues to the ability of FlhF to interact with either FliM-N or FlrA-HTH. None of these variants interacted with either FlrA-HTH or FliM-N (Fig. 3 *D* and *E*, respectively), consistent with FlrA and FliM sharing an interaction site on FlhG. To determine the in vivo effects of an FlhG mutant incapable of interacting with FliM and FlrA, we investigated the behavior of $FlhG_{K175E}$ in vivo (Fig. 3*F*). We introduced the corresponding substitution into *flhG* on the chromosome using a strain in which the flagellar filament can be fluorescently labeled by coupling of maleimide dyes to introduced cysteines in the flagellins (27) to visualize the number and localization of flagellar filaments. The $FlhG_{K175E}$ mutant had more polar flagella, phenocopying the hyperflagellated Δ*flhG* mutant. These findings highlight the importance of FlhG helices α6 and α7 as the interface with both FliM and FlrA. In contrast, the $FlhG_{D58A}$ variant, which promotes the ATP-dependent homodimeric state, led to a substantially reduced flagellation (from 55% in wt cells to 14% in the $FlhG_{D58A}$ mutant). This is probably due to increased inhibitory interaction between the FlhG homodimer and FlrA, in which FlrA is sequestered from its function as a transcriptional activator (Figs. 3*F* and 4*F*). This is confirmed by an FlhG variant containing both D58A and K175E substitutions, which phenocopies the hyperflagellation of the $FlhG_{K175E}$ strain and the *flhG* deletion strain (Fig. 3*F*). Although the $FlhG_{D58A\ K175E}$ variant exists as an ATP-dependent homodimer (D58A) required for FlrA interaction, it could no longer interact with FlrA (or FliM).

The FlhG-Binding Site at FlrA Impacts Flagellar Localization and Number. Next, we wanted to understand the impact of the interaction with FlhG on FlrA and the ramifications for *S. putrefaciens*

flagellation. We introduced a deletion of the FlhG-binding site in FlrA ($_{FlrA\Delta 389–409}$) in maleimide-labelable filament or hook background strains ($FlaAB_{cys}$, $FlgE_{cys}$) for quantification and localization. The $FlrA_{\Delta 389–409}$ strain assembled multiple flagella (2–8) localizing as single filaments or tufts at apparently random positions over the cell body (Fig. 4 *A* and *B* and *SI Appendix*, Fig. S6*B*). We next mutated selected amino acids within the FlhG-binding site, namely, E393R, R397E, D398R, L400E, and E408R. While mutation of the charged residues had little or no effect, the $FlrA_{L400E}$ strain showed the same major phenotype as the removal of the entire FlhG-binding site in our $FlrA_{\Delta 389–409}$ strain (Fig. 4*A* and *SI Appendix*, Fig. S6*A*), corroborating that this substitution uncouples FlhG-mediated regulation of FlrA activity. Also, an ectopic overexpression of FlhG in the $FlrA_{L400E}$ mutant leads to a delocalized hyperflagellation (Fig. 4*D*), corroborating that this substitution uncouples FlhG-mediated regulation of FlrA activity. These results confirmed that the FlhG-binding site in FlrA and, most importantly, the leucine residue at position 400—and therefore likely FlrA–FlhG interaction—are strictly required for normal flagellation of *S. putrefaciens*.

This phenotype resembled the phenotype of a mutant deleted in both *flhF* and *flhG*, but not that of an FlrA overexpression, which is polarly hyperflagellated (Fig. 4 *A* and *B* and *SI Appendix*, Fig. S6*B*). Disruption of the FlrA–FlhG interaction was also different from that of the synchronous overexpression of FlhF and FlhG or FlhG alone, which gradually diminished monopolar flagellation, resulting in mainly nonflagellated cells (Fig. 4 *A*, *B*, and *D*).

FlhG Down-Regulates FlrA Transcriptional Activity in a Negative Feedback Loop. Our results suggest that the ATP-dependent interaction of the FlhG dimer with FlrA affects the transcriptional activity of FlrA, which should be reflected in the transcription of

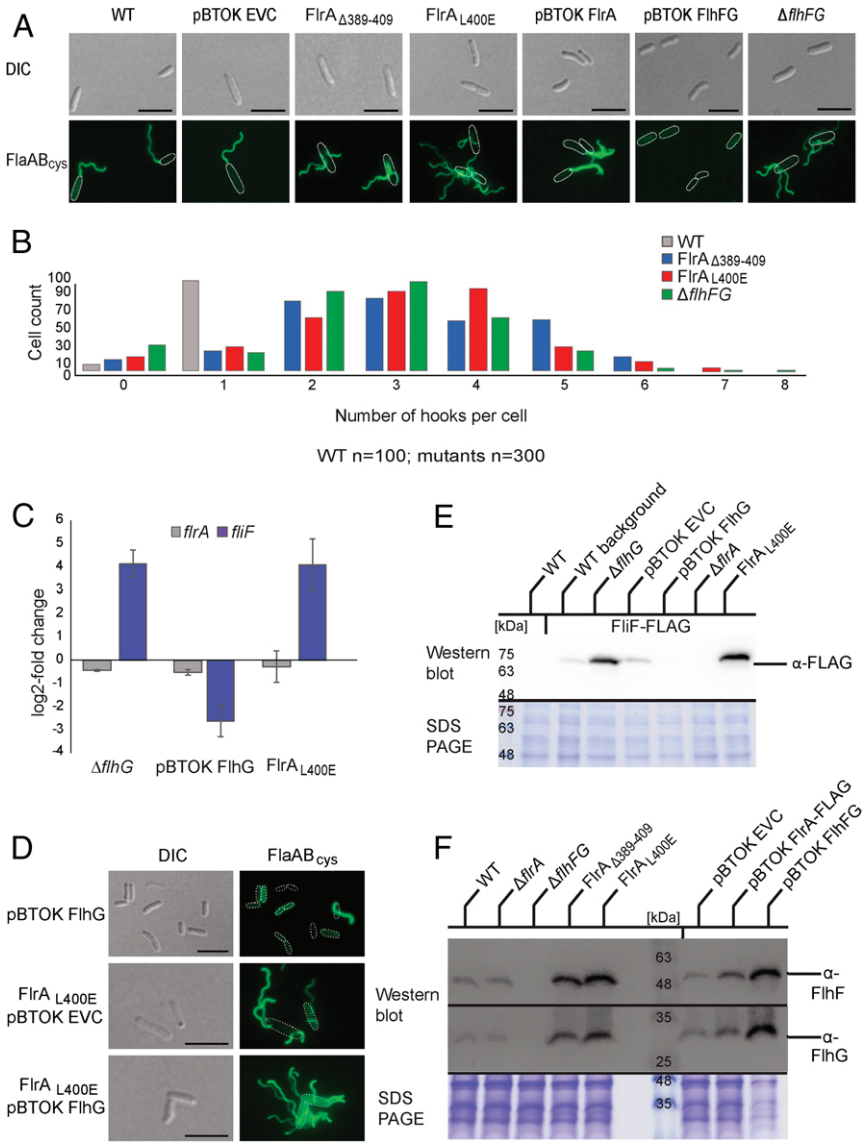

Fig. 4. FlrA–FlhG interaction affects transcriptional and spationumerical control of flagella. (*A*) Fluorescence microscopy images (Alexa Fluor 488 maleimide) with stained filaments and DIC images depicting FlrA mutants in the FlhG-binding interface with additional controls. (Scale bar, 5 μm.) (*B*) Quantification of the number of hooks per cell in *Shewanella putrefaciens* wt and hyperflagellation mutants (see *A* for corresponding fluorescence images). (*C*) qPCR data highlighting the close alignment of $FlrA_{L400E}$ and *flhG* deletion phenotypes, in comparison with a FlhG overexpression control. (*D*) Quantification of FLAG-tagged FlrA, FliM, and FlhG by Western blot highlights the threefold excess of FlhG in *S. putrefaciens* wt. (Scale bar, 5 μm.) (*E*) Fluorescence microscopy images (Alexa Fluor 488 maleimide) with stained filaments and DIC images depicting overexpression of FlhG in FlrA mutants in the FlhG-binding interface with additional controls. (*F*) Western blots depicting the increase of FlhG and FlhF protein levels in $FlrA_{L400E}$ and $FlrA_{\Delta 389–409}$ strains.

FlrA-regulated genes. One gene reported to be FlrA dependent is *fliF*, which encodes the protein that forms the flagellar MS ring, the chassis structure of the flagellar part located in the cytoplasmic membrane. In contrast, FlrA does not regulate its own expression (28). We quantified the transcript levels of *fliF* and *flrA* in strains lacking *flhG* or ectopically overexpressing *flhG* and in the $flrA_{L400E}$ mutant strain, in which FlhG–FlrA interaction is disrupted. Transcript levels of *flrA* were unaffected by the amounts of FlhG or its ability to interact with FlrA (Fig. 4*C*). In contrast, *fliF* transcript levels increased substantially in the absence of FlhG but decreased substantially upon overproduction of FlhG (Fig. 4*C*). In the $flrA_{L400E}$ mutant, *fliF* transcript levels were increased similarly to those of the *flhG* deletion (Fig. 4*C*), indicating that normal *fliF* expression depends on the ability of FlhG to interact with FlrA and not simply on the correct FlhG concentration. To confirm that the different levels in transcription are reflected at the protein level, we determined the cellular concentrations of FliF by Western blotting. To this end, we chromosomally replaced *fliF* with a hybrid gene featuring an additional FLAG affinity tag for detection of FliF. FLAG-tagged FliF was stably produced and fully supported flagellar function as measured by soft-agar motility (*SI Appendix*, Fig. S6*C*). Indeed, FliF production correlated with the corresponding transcription levels and increased by a factor of 5 in cells lacking FlhG (Δ*flhG*) or in which FlhG–FlrA interaction was disrupted ($FlrA_{L400E}$) (Fig. 4*E*).

FlrA had been reported to be a transcriptional activator of *flhF* and *flhG* as well as *fliF* (29), suggesting that FlhG may control its own production via interaction with FlrA. We investigated the effect of FlhG–FlrA interaction on the in vivo levels of FlhF and FlhG by quantitative Western blotting with antibodies directed against FlhF and FlhG (Fig. 4*F*). Disruption of the FlrA–FlhG interaction (i.e., $FlrA_{\Delta 389-409}$, $FlrA_{L400E}$) led to an approximately threefold increase in FlhF and FlhG levels (Fig. 4*F*). In this way FlhG has a means to exert control over the production of not only its own but also all of the other FlrA-dependent flagellar building blocks via its interaction with FlrA.

Discussion

The formation of a single polar flagellum requires complex spatiotemporal control of synthesis, i.e., shutting down the production of early flagellar building blocks upon completion of the corresponding structures to initiate the production of the next group of proteins (2). It has been shown that in most bacterial flagellar systems the transcription and production of one of the latest and definitely the most abundant building blocks, the flagellin, are regulated by an intricate mechanism that links completion of the previous structure, the flagellar hook, with flagellin production (30). This is achieved by placing the flagellin-encoding gene(s) under the control of a promotor, whose activity depends on an alternative sigma factor, FliA (σ28). FliA is kept inactive by its cognate anti-sigma factor (FlgM). When the flagellar hook reaches an appropriate length, as determined by the "tape measure" protein FliK (31), the flagellar type III secretion system (fT3SS) switches its specificity, removes the anti-sigma factor FlgM from the cell, and thereby releases FliA to start flagellin production. While this final step can be elegantly explained, the regulation of the initial step, involving the regulator of the flagellar number, the MinD-like ATPase FlhG, is by far less well understood.

Here we investigated the interaction between FlhG and its interaction partners FliM and FlrA in the polar flagellate *S. putrefaciens* using an array of in vitro and in vivo approaches. We found that the conserved N-terminal EIDAL motif of the flagellar C-ring component FliM interacts with FlhG as well as CheY (Fig. 5*A*). We also found that the transcriptional master regulator of flagellar biosynthesis, FlrA, a homolog of the FleQ protein, uses its linker between its AAA+ ATPase and DNA-binding HTH domain to interact with FlhG (Fig. 5*B*). Intriguingly, our results show that FliM and FlrA bind the same site on FlhG, helices α6 and α7. The major difference between the FlrA and FliM interaction is in the oligomeric state of FlhG, which can switch from monomer to dimer in an ATP-dependent manner (Fig. 5*C*). While the FliM interaction with FlhG is independent of nucleotides and binds monomeric FlhG, the FlrA interaction with FlhG requires the ATP-dependent FlhG dimer (Fig. 5 *A* and *B*). Our study also shows that the FlhG–FliM and FlhG-ATP–FlrA interactions occur with similar low–micromolar range binding strengths. Moreover, our study revealed that the interaction of FlhG with the linker of FlrA stimulates FlhG ATPase activity, which would drive dissociation of the homodimer to become monomers (Fig. 5*D*).

Its interaction with FliM is critical for FlhG to reach the cell pole at which flagellar biosynthesis occurs because FlhG does not localize to the cell pole in a *S. putrefaciens* strain producing a FliM lacking its N-terminal EIDAL motif. This means that assembly of the C ring is the factor that recruits FlhG to the pole. These findings also suggest that FlhG has a passive role and is not an active pole-marking protein. The FliM-mediated tethering of FlhG to the pole also implies that flagellar assembly transiently increases the concentration of FlhG at the pole. After recruitment to the pole, FliM incorporates into the assembling C ring, which should be accompanied by a release of FlhG (Fig. 5*I*). Support for this idea is provided by our cryotomographic experiments demonstrating that FlhG is neither crucial for proper C-ring assembly nor an integral part of the flagellum. The mechanism by which FlhG releases from FliM upon integration of the latter into the C ring is unknown. We speculate that the interaction of FliM with FliG involves conformational rearrangements triggering the release of FlhG from FliM. However, further studies need to address this relevant point.

The observation that the FliM interaction with FlhG is nucleotide independent also raises the question of at which point ATP-dependent FlhG dimerization occurs. Our study clarifies that ATP-dependent FlhG dimerization is prerequisite for its interaction with FlrA. Accumulation of dimeric FlhG therefore leads to suppression of flagellar assembly via suppressing the transcriptional activity of FlrA. This is supported by our results in which *flhG* deletion and the $FlrA_{L400E}$ variant led to an increase of the transcript for the flagellar MS-ring protein FliF being under the direct transcriptional control of FlrA. Removing FlhG or preventing its interaction with FlrA led to FlrA having a greater effect on transcription, as its activity is no longer repressed (Fig. 5*H*). These data suggest that the ATP-dependent FlhG dimer constantly interacts with FlrA, inhibiting FlrA transcriptional activity and therefore the production of flagellar components (Fig. 5*B*). Because FlhG interacts with the linker region connecting the AAA+ and HTH domains of FlrA, we suggest that this interaction either prevents FlrA from binding DNA or interferes with the dimer/hexamer equilibrium of FlrA, modulating its ability to interact with promoter regions. Structural studies of the *P. aeruginosa* FlrA homolog, FleQ, have shown that hexamerization occurs via its AAA+ domain (23). The proximity of the FlhG-binding site and the AAA+ domain of FlrA suggests that the FlrA interaction with dimeric FlhG leads to a shift from the transcriptionally active hexamer to the transcriptionally inactive dimer or vice versa (18, 23). Future studies will clarify the molecular consequences of interaction of FlhG for the ability of FlrA to bind and discriminate between different promoters.

Intriguingly, disruption of FliM and FlrA binding in the $FlhG_{K175E}$ mutant results in hyperflagellation, demonstrating that the binding site of FlrA and FliM on FlhG is crucial for limiting the number of flagella per cell (Fig. 5 *A*, *B*, and *F*). Moreover, combination of the FlhG K175A and D58A variations led to polar hyperflagellation, showing that although this variant

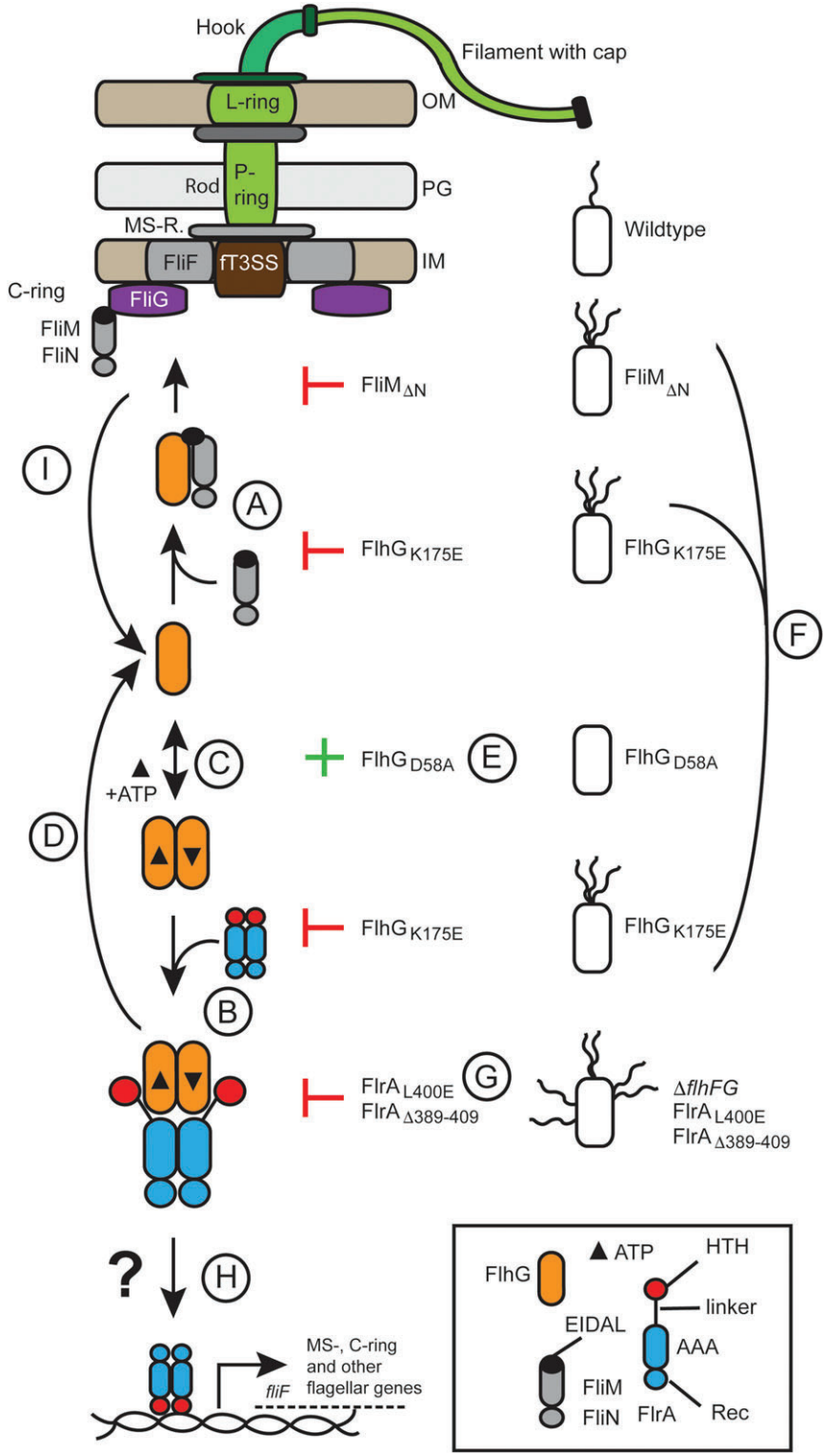

Fig. 5. ATP-dependent partner switch links flagellar C-ring assembly with gene expression. The color code is given in the legend. Abbreviations are OM, outer membrane; PG, peptidoglycan; IM, inner membrane; and fT3SS, flagellar type III secretion system. Further explanations for the steps indicated by "A" to "I" are given in *Discussion*.

is capable of forming ATP-dependent homodimers, it is unable to numerically regulate flagellar biosynthesis (Fig. 5 *A*–*C*). $FlhG_{D58A}$ alone led to the loss of flagella (Fig. 5*E*). However, disrupting the binding interface of FlhG in the linker of FlrA led to an entirely different outcome (Fig. 5*G*). Naively, the $FlrA_{\Delta 389–409}$ and $FlrA_{L400E}$ variants might be expected to phenocopy Δ*flhG* or $FlhG_{K175E}$. Unexpectedly, rather than showing polar hyperflagellation, these strains had multiple flagella randomly distributed over the cell surface, a phenotype reminiscent of Δ*flhF* or Δ*flhFG* strains. This suggests another layer of regulation at the level of FlrA

that also involves FlhF. Previous studies of *S. putrefaciens* and other polarly flagellated species and also amphitrichous and peritrichous flagellates support this by showing that FlhG interacts with FlhF through its N-terminal activator helix (14, 16) to simulate the FlhF GTPase. Thus, it is likely that the FlrA–FlhG interaction also indirectly impacts FlhF. This idea is supported by our quantification of the cellular levels of the FlhG and FlhF, showing that deletion of FlrA has no effect on the protein levels of FlhF and FlhG. However, deletion or variation of the FlhG-binding site on FlrA led to a substantial increase in levels of FlhF and FlhG. Taken together, these results show that the cellular levels of FlhF and FlhG are dependent on interaction of FlhG with FlrA. Thus, the $FlrA_{\Delta 389–409}$ and $FlrA_{L400E}$ variants result in higher levels of FlhG, which prevent FlhF from guiding flagella biosynthesis to the cell pole. Taken together, our study shows that the number of flagella per cell depends on a fine-tuned equilibrium of oligomeric states of the ATPases FlhG and FlrA and the availability of the flagella building block FliM to tether FlhG to the flagellar assembly point at the pole and therefore make FlhG unavailable to modulate FlrA (Fig. 5). It will be interesting to see how naturally occurring sequence changes in *flhF* and *flhG* in closely related species such as *Vibrio fischeri* and *P. putida,* which naturally produce multiple polar motors, affect this equilibrium.

More generally, our study suggests that assembly of the flagellar C ring significantly impacts the transcription of flagella building blocks and accessory regulators of flagella assembly, number, and localization. Depending on the progression of the C-ring assembly, FlhG is recruited to the cell pole, which in turn influences its ability to interact with the master transcriptional regulator FlrA and also the GTPase FlhF. These observations also suggest that our current understanding of how the flagellar assembly hierarchy is regulated through transcriptional tiers (reviewed in ref. 2) is incomplete and may be only one side of the coin. Thus, our study highlights how the physical assembly of a macromolecular machine regulates the production of its own building blocks.

Concluding Remarks and Open Questions. While our study provides a mechanistic framework underlying the numerical regulation of polar flagella, many questions remain unanswered. First, the FliM–FlhG interaction is critical for the determination of flagellar number because deletion of the FliM N terminus not only alleviates the polar localization of FlhG but also leads to hyperflagellation, phenocopying deletion of *flhG,* or overexpression of FlrA. This twist cannot be sufficiently explained by our current model (Fig. 5). It may be that the MTS of FlhG may play a substantial role in this process. The FliM-mediated shepherding of FlhG to the nascent polar flagellar structure may be prerequisite for the further interactions of FlhG (e.g., with FlhF) near the membrane. If this idea is correct, not only the cellular copy number of FlhG but also its subcellular localization is critical for its function in the numerical regulation of flagella. Another important but still not clarified question is how another round of flagellar synthesis is initiated. Our model suggests that FlhG autoregulates its own expression and production by binding to FlrA and interfering with its transcriptional activity. Thus, the next cycle of flagella production may be started by disruption of the FlhG–FlrA interaction or a short burst of FlrA expression to increase the amount of active FlrA. The underlying mechanism, the factors involved therein, and signals and timing remain unclear, and further experiments are required to address these questions.

Materials and Methods

HDX-MS. Samples for HDX-MS of *Sp*FlhG/*Sp*FliM/FliN were automatically prepared by a two-arm robotic autosampler (LEAP Technologies); 7.5 μL (50 μM) of *Sp*FlhG or the *Sp*FlhG/*Sp*FliM/FliN complex were mixed with 67.5 μL of D_2O-containing size exclusion chromatography (SEC) buffer to start H/D exchange. After incubation for 10, 30, 95, 1,000, and 10,000 s at 25 °C, 55 μL of the reaction were added to 55 μL quench buffer (400 mM KH_2PO_4/H_3PO_4, 2 M guanidine HCl, pH 2.2) kept at 1 °C, and 95 μL of the resulting mixture were immediately injected into an ACQUITY UPLC M-class system with HDX technology (Waters) (32). *Sp*FlhG was digested online with immobilized porcine pepsin at 12 °C at a 100 μL/min flow rate of water + 0.1% (vol/vol) formic acid, and the resulting peptic peptides were collected on a trap column (2 mm × 2 cm) filled with POROS 20 R2 material (Thermo Scientific) kept at 0.5 °C. After 3 min, the trap column was placed in line with an ACQUITY UPLC BEH C18 1.7 μm 1.0 × 100 mm column (Waters), and the peptides were eluted at 0.5 °C using a gradient of water + 0.1% formic acid (A) and acetonitrile + 0.1% formic acid (B) at a 30 μL/min flow rate, with a linear increase from 5 to 35% B within 7 min followed by a ramp to 85% B within 1 min and holding at 85% B for 2 min. Thereafter, the column was washed for 1 min at 95% B and equilibrated at 5% B for 5 min. Peptides were ionized by electrospray ionization at 250 °C source capillary temperature and a spray voltage of 3.0 kV. Mass spectra were acquired on a G2-Si HDMS mass spectrometer with ion mobility separation (Waters) over a range of 50 to 2,000 *m/z* in $HDMS^E$ or HDMS mode for undeuterated and deuterated samples, respectively (33, 34). Lock mass correction was performed with [Glu1]-fibrinopeptide B standard (Waters). Measurements were performed in triplicates. Between samples, the pepsin column was washed three times with 80 μL of 4% (vol/vol) acetonitrile and 0.5 M guanidine hydrochloride, and additionally, blank runs were performed between samples. Peptides were identified, and deuterium uptake was determined employing the PLGS and DynamX 3.0 softwares (both Waters) as described previously (35).

Samples for HDX-MS of $SpFlhG_{D58A}$/*Sp*FlrA-HTH were prepared manually. Prior to HDX, 50 μM $SpFlhG_{D58A}$ were incubated together with 1 mM ATP in the absence or presence of 100 μM $SpFlrA_1$-HTH for 1 min at 25 °C. H/D exchange was started by 10-fold dilution in D_2O-containing SEC buffer supplemented with 1 mM ATP. Undeuterated samples were prepared similarly by 10-fold dilution in H_2O-containing SEC buffer. After incubation for 30, 120, and 600 s at 25 °C, the reaction was stopped by the addition of an equal volume of ice-cold quench buffer (400 mM KH_2PO_4/H_3PO_4, pH 2.2) directly injected into an ACQUITY UPLC M-class system with HDX technology (Waters) and analyzed as described above.

Protein Expression and Purification for Pulldowns, ATPase Assays, HDX-MS, MST. pET and pGAT vectors were used for the protein constructs that were overexpressed in *Escherichia coli* BL21 (DE3) competent cells. The following genes from *S. putrefaciens* CN-32 were used as templates for constructs mentioned in the text: Sputcn32_2580 (FlrA), Sputcn32_2569 (FliM), Sputcn_2568 (FliN), Sputcn2560 (FlhG). Cell cultures were grown in lysogeny broth medium at 30 °C overnight and shaken at 180 rpm. One percent lactose monohydrate (wt/vol) was used for induction. Cells were harvested and lysed by microfluidizer (M110-L, Microfluidics) and centrifuged to pellet cell debris. The supernatant was then loaded onto a GE Healthcare GSTrapFF or HisTrapFF affinity column (for GST-tagged and His-tagged proteins, respectively). For His-tagged proteins, the lysis and wash buffer contained 20 mM HEPES (4-(2-hydroxyethyl)-1-piperazine ethanesulfonic acid) (pH 8.0), 250 mM NaCl, 20 mM KCl, 20 mM $MgCl_2$, and 40 mM imidazole, while the imidazole concentration in the elution buffer was increased to 500 mM. For GST-tagged proteins, the lysis and wash buffer contained 20 mM HEPES (pH 7.5), 200 mM NaCl, 20 mM $MgCl_2$, and 20 mM KCl. Elution was carried out with 50 mM Tris (pH 8.0), 20 mM glutathione (GSH) buffer. After elution, proteins were purified by SEC using S200 Sepharose columns and GE Lifesciences AKTA Prime and Purifier systems. After purification, the proteins were concentrated using Amicon Ultra-15 spin concentrators.

GST Pulldown Assays. Spin columns and filters from MobiTec were used for the assays. Thirty microliters of a GST-Sepharose bead suspension (GE Healthcare) were used, loaded into the assembled spin column and resuspended in 500 μL HEPES buffer (20 mM HEPES, 200 mM NaCl, 20 mM $MgCl_2$, 20 mM KCl, pH 7.5, 0.6 μM Tween20). The suspension was then centrifuged for 1 min at 4,000 rpm; then the GST-tagged protein (1 nmol) was immobilized for 15 min on a rotation machine and then centrifuged for 1 min at 4,000 rpm, washed with 500 μL HEPESTween20 buffer, and centrifuged again under the same conditions. The interaction partner was then loaded (10 nmol); they were incubated together on a rotation machine for 30 min and then washed three times with 500 μL HEPES-Tween20 buffer. The elution was performed with 40 μL of a buffer containing 50 mM Tris and 20 mM GSH (pH 8.0). All of the samples were then separated by sodium dodecylsulfate–polyacrylamide gel electrophoresis and stained with Coomassie blue.

FlhG ATPase Activity. The ATPase activity of FlhG was determined by incubating 10 μM FlhG without or together with 10 μM FlrA-HTH in SEC buffer (20 mM HEPES, pH 7.5, 20 mM $MgCl_2$, 20 mM KCl, 200 mM NaCl) supplemented with 0.05, 0.1, 0.25, 0.5, 0.75, 1, 2.5, and 5 mM ATP. The reactions were incubated at 37 °C for 12, 24, 36, 48, and 60 min (without FlrA-HTH) or 3, 6, 9, 12, and 15 min (with FlrA-HTH) and quenched by addition of two volume parts of chloroform, followed by thorough mixing for 15 s, heat treatment at 95 °C for 15 s, and flash freezing in liquid nitrogen. While thawing, samples were centrifuged (17,300 × *g*, 30 min, 4 °C); the aqueous phase was removed and subjected to high-performance liquid chromatography analysis. Measurements were conducted on an Agilent 1260 Series system (Agilent Technologies) equipped with a C18 column (EC 250/4.6 Nucleodur HTec 3 μM; Macherey-Nagel). Nucleotides were eluted at a 0.8 mL/min flow rate with a buffer containing 50 mM KH_2PO_4, 50 mM K_2HPO_4, 10 mM tetrabutylammonium bromide, and 15% (vol/vol) acetonitrile and detected at a 260 nm wavelength, in agreement with standards of ADP and ATP. Data analysis was performed with Prism version 6.04 for Windows (GraphPad Software). The velocity of ATPase activity was obtained by linear regression of the amount of ADP quantified after different incubation times. Kinetic parameters (K_m, V_{max}) were obtained from the fit of the v/S characteristic according to the equation $v = V_{max}[S]/(K_m + [S])$, where [S] is the concentration of substrate ATP.

Y2H Assays. For Y2H interaction assays, plasmids expressing the FlhG bait protein, fused to the Gal4 DNA-binding domain, and prey proteins, fused to the Gal4 activation domain, were cotransformed into the reporter strain PJ69-4A (36). Y2H interactions were documented by spotting representative transformants in 10-fold serial dilution steps onto SC-Leu-Trp (-LT), SC-His-Leu-Trp (-HLT; *HIS3* reporter), and SC-Ade-Leu-Trp (-ALT; *ADE2* reporter) plates, which were incubated for 3 d at 30 °C. Growth on -HLT plates is indicative of a weak or moderate interaction, and only relatively strong interactions also permit growth on -ALT plates.

RNA Isolation and qPCR. Total RNA of exponentially growing *Shewanella* cells (optical density [OD] at a wavelength of 600 nm = 0.5, three biological replicates) were extracted using a Direct-zol RNA MiniPrep (Zymo Research) according to the manufacturer's instructions. The concentration of RNA was measured at 260 nm. Residual DNA was removed with a Turbo DNA-free Kit (Thermo Fisher Scientific) according to the manufacturer's instructions. RNA samples were stored at −80 °C. For the qPCR a C1000 Thermal Cycler with the CFX96 Real-Time System (Bio-Rad) and strips of low-profile tubes (white) with ultraclear caps (Thermo Fisher Scientific) were used for PCR amplification. For the qPCR, Takyon no ROX SYBR Mastermix dTTP Blue (Eurogentec) and a Takyon One-Step Kit Converter (Eurogentec) were used in a reaction volume of 20 μL containing 40 ng of RNA template, 0.25 mM of both forward and reverse primers, 0.2 μL of Euroscript II RT/RNase inhibitor, and 10 μL of 2× Takyon mastermix. Cycling conditions were as follows: a reverse transcription step at 48 °C for 10 min and 95 °C for 3 min, then 40 cycles of 95 °C for 5 s and 60 °C for 20 s. RNA samples treated without reverse transcriptase were used to test for DNA contaminations in the extracted RNA. The cycle threshold (Ct) was determined automatically after 40 cycles (Real-Time CFX Manager 2.1, Bio-Rad). Ct values for each gene of interest were normalized against the Ct value of *gyrA* (Sputcn32_2070). Primer efficiencies and relative transcript levels were determined according to Pfaffl (37) and used to estimate the differences in transcript amounts of the genes of interest.

Western Blot Analysis. Production and stability of the fusions were determined by Western blot analyses. Protein lysates were prepared from exponentially growing cultures. Collection of protein samples, protein separation, and immunoblot detection were essentially carried out as described earlier (19). To detect the proteins, monoclonal, horseradish peroxidase–conjugated antibody raised against the FLAG tag (Sigma Aldrich) and polyclonal antibodies raised against FlhG or FlhF in a dilution of 1:1,000 were used. Secondary anti-rabbit immunoglobulin G (IgG)–alkaline phosphatase antibody was used at a dilution of 1:20,000 to detect FlhG and FlhF antibodies. Signals were detected with SuperSignal West Pico PLUS Chemiluminescent Substrate (Thermo Scientific) or CDP-Star chemiluminescent substrate (Roche Diagnostics) and were documented using a Fusion-SL chemiluminescent imager (Peqlab).

Strain Constructions (Fluorescence Microscopy Experiments). Genetic manipulations of *S. putrefaciens* CN-32 were introduced into the genome to replace the native gene locus. The in-frame deletions or chromosomal integration of gene variants or fusions were obtained by sequential double homologous recombination using the suicide plasmid pNTPS-138-R6K carried out essentially as previously described. Vectors were transferred into CN-32 cells via conjugation using *E. coli* WM3064 as a donor. All strains are listed in *SI Appendix*, Table 1.

Flagellar and Hook Staining. Fluorescent staining of flagellar filaments (CN-32 $FlaAB_1$-Cys; ref. 27) or hook structures ($FlgE_1$-Cys) was essentially carried out on exponentially growing cells as previously described (38) using Alexa Fluor 488 maleimide (Thermo Fisher Scientific).

Fluorescence Microscopy. *Shewanella* strains were cultured to midexponential phase before imaging. There were 2.5 μL of culture spotted on an agarose pad. Fluorescence images were recorded by a DMI6000B inverse microscope (Leica) equipped with a pco.edge sCMOS camera (PCO) and an HCX PL APO 100×/1.4 differential interference contrast (DIC) objective using the VisiView software (Visitron Systems GmbH). Images were further processed using ImageJ 1.52v software (NIH) and Affinity Designer 1.7v (Serif).

MST. MST was performed on a Monolith NT.115 (NanoTemper Technologies GmbH) at 21 °C (red light-emitting diode power was set to 70%, and infrared laser power was set to 25%) (39). The target protein (50 μM) was labeled with the dye NT 647 according to the supplier's protocol (NanoTemper Technologies); 200 nM of the labeled target protein were titrated with the putative interaction partner starting from a concentration of 0.5 mM in Buffer C (20 mM HEPES, pH 7.5, 200 mM NaCl). To each measurement, Tween20 (Sigma) was added to a final concentration of 0.05 mM. At least nine independent MST experiments were recorded at 680 nm and processed by NanoTemper Analysis 1.2.009. Origin8G was employed for data fitting and determination of the dissociation constant.

Homology Modeling. Protein homology modeling was performed using the SWISS-MODEL server (40). The structures *Geobacillus thermodenitrificans* FlhG (Protein Data Bank [PDB] ID codes 4RZ2 and 4RZ3) and *Brucella abortus* NtrX (PDB ID code 5M7N) served as templates for modeling FlhG and FlrA, respectively.

Electron Cryotomography. *S. putrefaciens* CN-32 wt and Δ*flhG* strains were cultivated from freezer stocks in LB medium at 30 °C. Prior to vitrification, strains were incubated overnight and subcultured until reaching the exponential growth phase (OD600 of ∼0.5). Cells were subsequently pelleted and resuspended to an OD600 of ∼13. Quantifoil R2/2 grids (200 mesh) (Quantifoil Micro Tools GmbH) were glow discharged for 60 s at 10 mA, and a solution of 10 nm colloidal gold in 1% (wt/vol) bovine serum albumin was pelleted and mixed with 30 μL cells immediately before plunge freezing. A 3 μL droplet of this sample solution was applied to the glow-discharged electron microscopy grid; the grid was blotted and plunge frozen into a liquid ethane–propane mixture using a Vitrobot plunge-freezing robot (FEI Company) with a wait time of 60 s, a blot time of 4 s, and blot offsets of −3 mm. Grids were stored under liquid nitrogen until data collection. Tilt series were collected on a 200 kV FEI Tecnai TF20 FEG transmission electron microscope (FEI Company) equipped with a Falcon II direct electron detector camera (FEI Company) using Gatan 914 or 626 cryoholders. Tilt series were recorded from −54° to +54° with an increment of 3° collected defocus between −3 and −6 μm using Leginon automated data collection software (41) at a nominal magnification of 25,000× and were binned four times to a final pixel size of 0.828 nm. Cumulative doses of ∼120 e−/$Å^2$ over the tilt series were used. Overnight data collection was facilitated by the addition of a 3 L cold-trap Dewar flask and automated refilling of the Dewar cryoholder triggered by a custom-written Leginon node interfaced with a computer-controlled liquid nitrogen pump (Norhof LN2 Systems).

Subtomogram Averaging. Tomograms were reconstructed automatically using RAPTOR (42) and the IMOD package (43). Low-defocus images were low-pass filtered to remove data beyond 3.5 nm^{-1}. Positions of flagellar motors in tomograms were initially aligned manually along their rotational axes. The particle estimation for electron tomography (PEET) package was used for iterative subtomogram extraction, fine alignment, and averaging (44). Resolution was estimated by Fourier shell correlation (FSC) by correlating the two halves of the dataset using FSC.

Data Availability. All data supporting the findings of this study are included in this paper and *SI Appendix*.

ACKNOWLEDGMENTS. We thank Sabrina Henche and Jan S. Schuhmacher for their contributions in the beginning of this work, Ulrike Ruppert for excellent technical support, and Paul Simpson from the Imperial College Centre for Structural Biology for electron microscopy assistance. The Landes Offensive zur Entwicklung wissenschaftlich-ökonomischer Exzellenz program of the state of Hesse (to G.B.), the German Research Foundation (DFG) (Project 269423233 - TRR 174 to G.B., R.B., and K.M.T.), the DFG Core Facility for Interaction, Dynamics and Macromolecular Assembly Structure (to G.B.), and a DFG Fellowship (to F.R.), and the UK Medical Research Council (Grant MR/P019374/1 to M.B.) supported this work.

1. F. Altegoer, G. Bange, Undiscovered regions on the molecular landscape of flagellar assembly. *Curr. Opin. Microbiol.* **28**, 98–105 (2015).
2. F. F. Chevance, K. T. Hughes, Coordinating assembly of a bacterial macromolecular machine. *Nat. Rev. Microbiol.* **6**, 455–465 (2008).
3. J. S. Schuhmacher, K. M. Thormann, G. Bange, How bacteria maintain location and number of flagella? *FEMS Microbiol. Rev.* **39**, 812–822 (2015).
4. B. I. Kazmierczak, D. R. Hendrixson, Spatial and numerical regulation of flagellar biosynthesis in polarly flagellated bacteria. *Mol. Microbiol.* **88**, 655–663 (2013).
5. N. Dasgupta, S. K. Arora, R. Ramphal, fleN, a gene that regulates flagellar number in Pseudomonas aeruginosa. *J. Bacteriol.* **182**, 357–364 (2000).
6. N. E. Correa, F. Peng, K. E. Klose, Roles of the regulatory proteins FlhF and FlhG in the Vibrio cholerae flagellar transcription hierarchy. *J. Bacteriol.* **187**, 6324–6332 (2005).
7. A. Kusumoto *et al*., Regulation of polar flagellar number by the flhF and flhG genes in Vibrio alginolyticus. *J. Biochem.* **139**, 113–121 (2006).
8. J. S. Schuhmacher *et al*., MinD-like ATPase FlhG effects location and number of bacterial flagella during C-ring assembly. *Proc. Natl. Acad. Sci. U.S.A.* **112**, 3092–3097 (2015).
9. C. J. Gulbronson *et al*., FlhG employs diverse intrinsic domains and influences FlhF GTPase activity to numerically regulate polar flagellar biogenesis in Campylobacter jejuni. *Mol. Microbiol.* **99**, 291–306 (2016).
10. B. P. Chanchal, P. Banerjee, D. Jain, ATP-induced structural remodeling in the anti-activator FleN enables formation of the functional dimeric form. *Structure* **25**, 243–252 (2017).
11. M. Balaban, D. R. Hendrixson, Polar flagellar biosynthesis and a regulator of flagellar number influence spatial parameters of cell division in Campylobacter jejuni. *PLoS Pathog.* **7**, e1002420 (2011).
12. T. H. Szeto, S. L. Rowland, C. L. Habrukowich, G. F. King, The MinD membrane targeting sequence is a transplantable lipid-binding helix. *J. Biol. Chem.* **278**, 40050–40056 (2003).
13. H. Zhou, J. Lutkenhaus, Membrane binding by MinD involves insertion of hydrophobic residues within the C-terminal amphipathic helix into the bilayer. *J. Bacteriol.* **185**, 4326–4335 (2003).
14. G. Bange *et al*., Structural basis for the molecular evolution of SRP-GTPase activation by protein. *Nat. Struct. Mol. Biol.* **18**, 1376–1380 (2011).
15. A. Kusumoto *et al*., Collaboration of FlhF and FlhG to regulate polar-flagella number and localization in Vibrio alginolyticus. *Microbiology* **154**, 1390–1399 (2008).
16. F. Rossmann *et al*., The role of FlhF and HubP as polar landmark proteins in Shewanella putrefaciens CN-32. *Mol. Microbiol.* **98**, 727–742 (2015).
17. N. Dasgupta, R. Ramphal, Interaction of the antiactivator FleN with the transcriptional activator FleQ regulates flagellar number in Pseudomonas aeruginosa. *J. Bacteriol.* **183**, 6636–6644 (2001).
18. C. Baraquet, C. S. Harwood, Cyclic diguanosine monophosphate represses bacterial flagella synthesis by interacting with the Walker A motif of the enhancer-binding protein FleQ. *Proc. Natl. Acad. Sci. U.S.A.* **110**, 18478–18483 (2013).
19. S. Bubendorfer *et al*., Specificity of motor components in the dual flagellar system of Shewanella putrefaciens CN-32. *Mol. Microbiol.* **83**, 335–350 (2012).
20. A. Paulick *et al*., Dual stator dynamics in the Shewanella oneidensis MR-1 flagellar motor. *Mol. Microbiol.* **96**, 993–1001 (2015).
21. M. Kaplan *et al*., In situ imaging of the bacterial flagellar motor disassembly and assembly processes. *EMBO J.* **38**, e100957 (2019).
22. J. L. Ferreira *et al*., γ-proteobacteria eject their polar flagella under nutrient depletion, retaining flagellar motor relic structures. *PLoS Biol.* **17**, e3000165 (2019).
23. B. Y. Matsuyama *et al*., Mechanistic insights into c-di-GMP-dependent control of the biofilm regulator FleQ from Pseudomonas aeruginosa. *Proc. Natl. Acad. Sci. U.S.A.* **113**, E209–E218 (2016).
24. S. K. Arora, B. W. Ritchings, E. C. Almira, S. Lory, R. Ramphal, A transcriptional activator, FleQ, regulates mucin adhesion and flagellar gene expression in Pseudomonas aeruginosa in a cascade manner. *J. Bacteriol.* **179**, 5574–5581 (1997).
25. C. Baraquet, K. Murakami, M. R. Parsek, C. S. Harwood, The FleQ protein from Pseudomonas aeruginosa functions as both a repressor and an activator to control gene expression from the pel operon promoter in response to c-di-GMP. *Nucleic Acids Res.* **40**, 7207–7218 (2012).
26. D. Houde, S. A. Berkowitz, J. R. Engen, The utility of hydrogen/deuterium exchange mass spectrometry in biopharmaceutical comparability studies. *J. Pharm. Sci.* **100**, 2071–2086 (2011).
27. M. J. Kühn, F. K. Schmidt, B. Eckhardt, K. M. Thormann, Bacteria exploit a polymorphic instability of the flagellar filament to escape from traps. *Proc. Natl. Acad. Sci. U.S.A.* **114**, 6340–6345 (2017).
28. L. Wu, J. Wang, P. Tang, H. Chen, H. Gao, Genetic and molecular characterization of flagellar assembly in Shewanella oneidensis. *PLoS One* **6**, e21479 (2011).
29. M. Shi, T. Gao, L. Ju, Y. Yao, H. Gao, Effects of FlrBC on flagellar biosynthesis of Shewanella oneidensis. *Mol. Microbiol.* **93**, 1269–1283 (2014).
30. K. T. Hughes, K. L. Gillen, M. J. Semon, J. E. Karlinsey, Sensing structural intermediates in bacterial flagellar assembly by export of a negative regulator. *Science* **262**, 1277–1280 (1993).
31. M. Erhardt, H. M. Singer, D. H. Wee, J. P. Keener, K. T. Hughes, An infrequent molecular ruler controls flagellar hook length in Salmonella enterica. *EMBO J.* **30**, 2948–2961 (2011).
32. T. E. Wales, K. E. Fadgen, G. C. Gerhardt, J. R. Engen, High-speed and high-resolution UPLC separation at zero degrees Celsius. *Anal. Chem.* **80**, 6815–6820 (2008).
33. S. J. Geromanos *et al*., The detection, correlation, and comparison of peptide precursor and product ions from data independent LC-MS with data dependant LC-MS/MS. *Proteomics* **9**, 1683–1695 (2009).
34. G. Z. Li *et al*., Database searching and accounting of multiplexed precursor and product ion spectra from the data independent analysis of simple and complex peptide mixtures. *Proteomics* **9**, 1696–1719 (2009).
35. M. Osorio-Valeriano *et al*., ParB-type DNA segregation proteins are CTP-dependent molecular switches. *Cell* **179**, 1512–1524.e15 (2019).
36. P. James, J. Halladay, E. A. Craig, Genomic libraries and a host strain designed for highly efficient two-hybrid selection in yeast. *Genetics* **144**, 1425–1436 (1996).
37. M .W. Pfaffl, A new mathematical model for relative quantification in real-time RT-PCR. *Nucleic Acids Res.* **29**, e45 (2001).
38. M. E. Heimbrook, W. L. Wang, G. Campbell, Staining bacterial flagella easily. *J. Clin. Microbiol.* **27**, 2612–2615 (1989).
39. M. Jerabek-Willemsen, C. J. Wienken, D. Braun, P. Baaske, S. Duhr, Molecular interaction studies using microscale thermophoresis. *Assay Drug Dev. Technol.* **9**, 342–353 (2011).
40. M. Bertoni, F. Kiefer, M. Biasini, L. Bordoli, T. Schwede, Modeling protein quaternary structure of homo- and hetero-oligomers beyond binary interactions by homology. *Sci. Rep.* **7**, 10480 (2017).
41. C. Suloway *et al*., Fully automated, sequential tilt-series acquisition with Leginon. *J. Struct. Biol.* **167**, 11–18 (2009).
42. F. Amat *et al*., Markov random field based automatic image alignment for electron tomography. *J. Struct. Biol.* **161**, 260–275 (2008).
43. J. R. Kremer, D. N. Mastronarde, J. R. McIntosh, Computer visualization of three-dimensional image data using IMOD. *J. Struct. Biol.* **116**, 71–76 (1996).
44. D. Nicastro *et al*., The molecular architecture of axonemes revealed by cryoelectron tomography. *Science* **313**, 944–948 (2006).